Supporting Information

Single-Atomic Ruthenium Dispersion Promoting Photoelectrochemical Water Oxidation Activity of CeO_x Catalyst on Doped TiO_2 Nanorods Photoanode

Debashish Pal,[1] Debayan Mondal,[2] Dipanjan Maity,[3] Debasis De,[4] Mukhesh K. Ganesha,[5] Ashutosh K. Singh,[5] and Gobinda Gopal Khan [1,*]

[1] Department of Material Science and Engineering, Tripura University (A Central University), Suryamaninagar, Agartala, Tripura 799 022, India

[2] Department of Condensed Matter Physics and Material Sciences, S. N. Bose National Centre for Basic Sciences, Block JD, Sector-III, Salt Lake, Kolkata, West Bengal 700 106, India

[3] Chemistry and Physics of Materials Unit, Jawaharlal Nehru Centre for Advanced Scientific Research, Jakkur, Bengaluru 560 064, India

[4] Energy Institute, Bengaluru, (Centre of Rajiv Gandhi Institute of Petroleum Technology), International Airport Road, Vidyanagar, Bengaluru 562 157, Karnataka, India

[5] Centre for Nano and Soft Matter Sciences (CeNS), Bengaluru 562 162, Karnataka, India

Corresponding author e-mail: G G Khan: gobinda.gk@gmail.com, gobindakhan@tripurauniv.ac.in

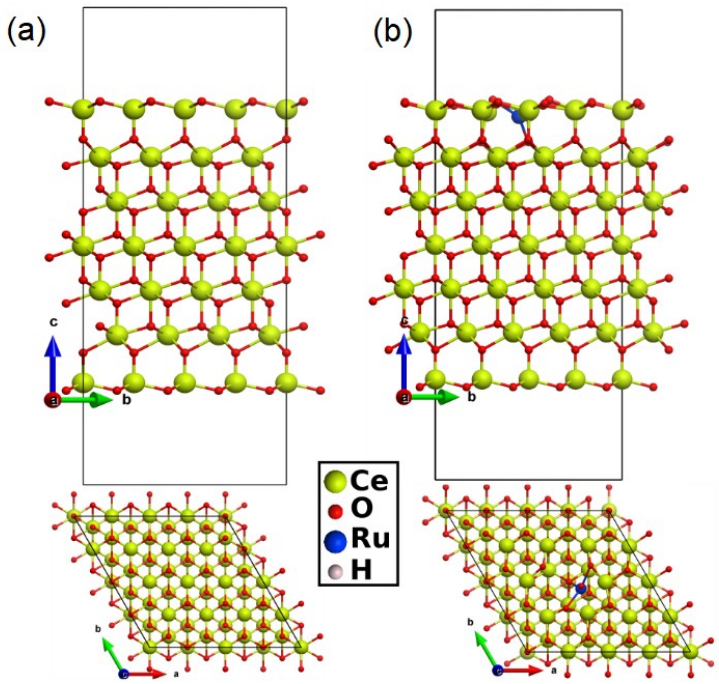

Fig. S1 Side view (upper panel) and top view (lower panel) of the optimized (a) CeO_2 (111) and (b) Ru:CeO_2 (111) surfaces.

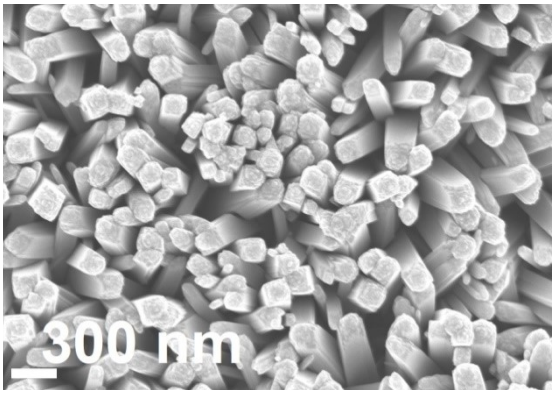

Fig. S2 Top view FESEM image of the Sb-TiO_2 NRs.

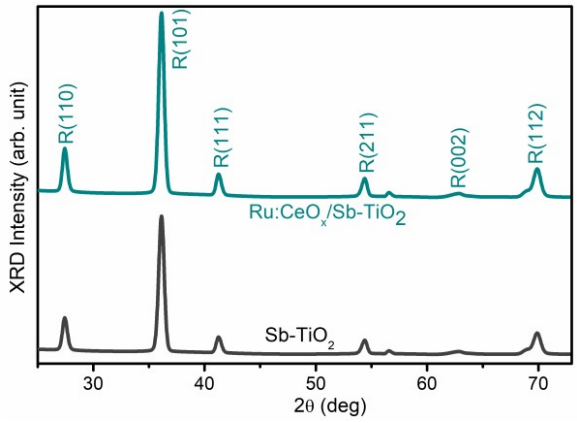

Fig. S3 GI-XRD patterns of the Ru:CeO_x/Sb-TiO_2 and Sb-TiO_2 NRs.

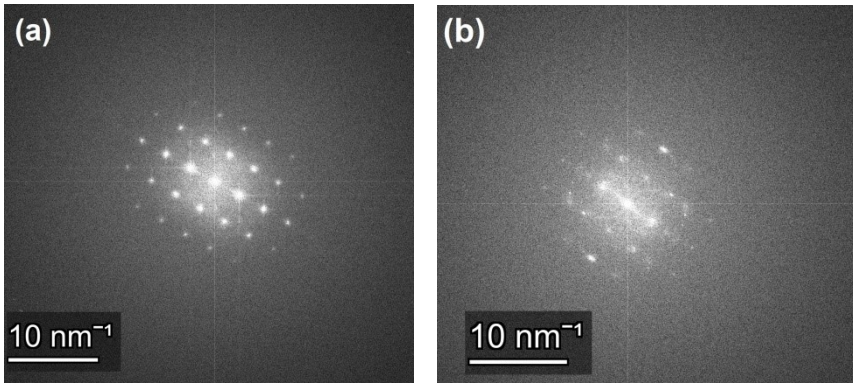

Fig. S4 The diffraction patterns via fast Fourier transformation (FFT) of TiO_2 (a) and CeO_x (CeO_2) (b).

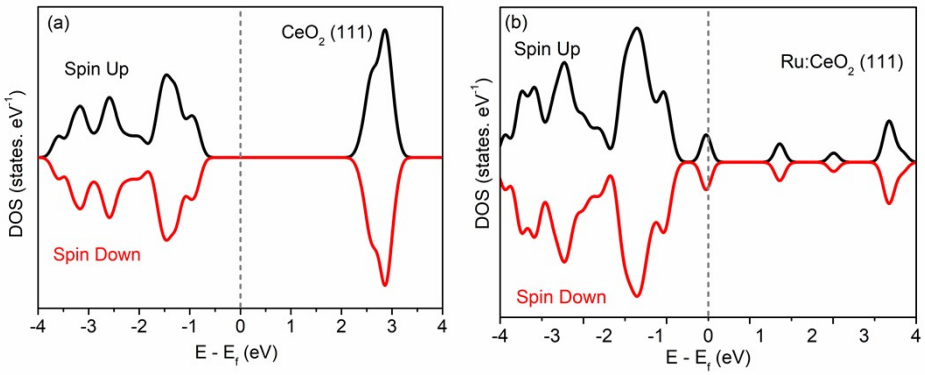

Fig. S5 Spin-up and spin-down total DOS of (a) CeO_2 (111) surface and (b) Ru:CeO_2 (111) surface.

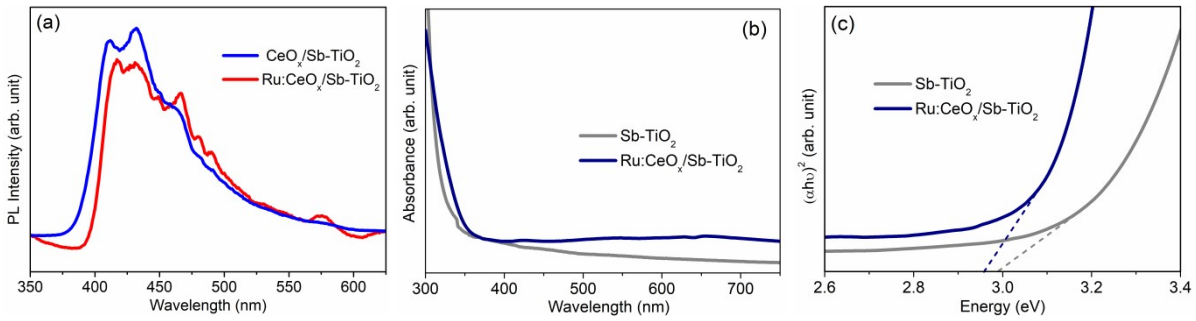

Fig. S6 (a) Room temperature steady-state PL emission spectra of CeO_x/Sb-TiO_2 and Ru:CeO_x/Sb-TiO_2. The UV-Vis absorbance spectra (a) and Kubelka-Munk plots (b) of the Ru:CeO_x/Sb-TiO_2 and Sb-TiO_2 NRs.

TRPL study

The as-obtained TRPL curves were fitted with the biexponential function of time [1,2]:

$$F(t) = A_1 e^{-1/\tau_1} + A_2 e^{-1/\tau_2} + y_0 \qquad (1)$$

Where τ_1 and τ_2 are the time constant related to fast and slow decay process, respectively.

The average recombination lifetime, reflecting the overall emission decay behaviour of the photoanodes was calculated as [1]:

$$\tau_{av} = \frac{\sum A_i \tau_i^2}{\sum A_i \tau_i}, \text{ where i = 1 and 2} \qquad (2)$$

Table S1 Decay parameters and the average lifetime of the TRPL decay curves for different photoanodes.

Photoanodes	τ_1 (ns)	τ_2 (ns)	A_1(%)	A_2(%)	τ_{ave} (ns)	χ^2
Sb-TiO_2	0.48	3.3	77.6	22.4	2.4	1.1
Ru:CeO_x/Sb-TiO_2	0.92	5.6	71.1	28.9	4.3	0.98

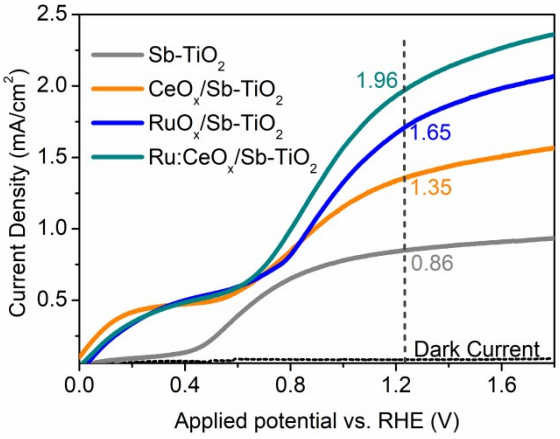

Fig. S7 *J-V* plots of the Sb-TiO_2, CeO_x/Sb-TiO_2, RuO_x/Sb-TiO_2 and Ru:CeO_x/Sb-TiO_2 photoanodes.

Calculation of η_{inj} and η_{sep}

The water splitting photocurrent density (J_{H_2O}) can be measured as [3]:

$$J_{H_2O} = J_{abs} \times \eta_{sep} \times \eta_{inj} \qquad (3)$$

Where, J_{abs} is the photocurrent density considering 100% photoconversion efficiency of absorbed irradiation. η_{sep} and η_{inj} represents photogenerated carriers separation, and the charge injection efficiency, respectively.

Hence, the highest J_{abs}, can be calculated as [4]:

$$J_{abs} = \int_{200\,nm}^{800\,nm} \frac{\lambda}{1240} \times \eta_{LHE}(\lambda) \times AM\ 1.5\ \psi(\lambda) d\lambda \qquad (4)$$

Where, $\eta_{LHE}(\lambda) = 1 - 10^{-A(\lambda)}$ is the light harvesting efficiency, A(λ) is the absorbance at a specific wavelength and AM 1.5ψ(λ) is the irradiance of simulated solar spectrum.

In order to determine η_{sep} and η_{inj} an 0.5M of hole scavenger (Na_2SO_3) was added to the 0.5M Na_2SO_4 electrolyte. Assuming that the presence of hole scavenger enhances injection efficiency to 100%, the charge separation and injection efficiencies can be calculated as [5,6]:

$$\eta_{sep} = \frac{J_{Na_2SO_3}}{J_{abs}} \qquad (5)$$

$$\eta_{inj} = \frac{J_{H_2O}}{J_{Na_2SO_3}} \qquad (6)$$

Photovoltage decay

A bi-exponential function having two time constants (τ_1 and τ_2) was fitted to the normalised OCP data to determine the decay lifetime of the charge carriers for the photoanodes [7]:

$$y(t) = A_0 + A_1 \exp\left(\frac{-t}{\tau_1}\right) + A_2 \exp\left(\frac{-t}{\tau_2}\right) \qquad (7)$$

where, τ_1 and τ_2 are the band-to-band and band-to-surface states charge recombination time components, respectively. The harmonic mean of τ_1 and τ_2 is calculated as:

$$t_m = \frac{\tau_1 \tau_2}{\tau_1 + \tau_2} \qquad (8)$$

The total half-life time is: $\ln(2\tau_m)$.

Table S2 Calculated values of harmonic mean and half-life of charge carriers.

Photoelectrode	τ_1	τ_2	τ_m	$\ln(2\tau_m)$
Sb-TiO_2	42.4	6.6	5.7	2.4
Ru:CeO_x/Sb-TiO_2	11.4	2.8	2.2	1.5

MS study

The flat band potential (E_{fb}) of the photoanodes was determined using the Mott-Schottky (M-S) equation [8]:

$$\frac{1}{C_s^2} = \frac{2}{e\varepsilon\varepsilon_0 A^2 N_d}\left(E - E_{fb} - \frac{k_B T}{e}\right) \qquad (9)$$

where, C_s is the space charge capacitance, e is the elementary charge (1.6×10^{-19} C), ε is the

dielectric constant of the semiconductor photoanode (170, rutile TiO_2) [9,10], ε_0 the free space permittivity (8.86×10^{-12} F m^{-1}), A is the geometrical area of the electrode, N_d is the carrier density, E is the applied potential, k_B the Boltzmann's constant (1.38×10^{-23} JK^{-1}), and T is the temperature in absolute scale.

The charge carrier density (N_d) of the photoanodes is also estimated from the slope of the linear part of the Mott−Schottky plots using the following equation [11]:

$$N_d = (2/e\varepsilon\varepsilon_0 A^2)[d(1/C_s^2)/dE]^{-1} \quad (10)$$

The depletion layer width (W_{dep}) of the photoanodes can be calculated as [12]:

$$W_{dep} = \sqrt{2\,\varepsilon\,\varepsilon_0 (V - V_{fb})/\,e\,N_d} \quad (11)$$

Where, V is the applied potential.

IPCE study

The incident-photon-to-current conversion efficiency (IPCE) of the photoanodes was conducted at 1.23V vs. RHE under AM 1.5 G illumination. As shown in Fig. 2b, the IPCE value of the Ru:CeO_x/Sb-TiO_2 photoanode is higher than that of the Sb-TiO_2 throughout the measured wavelength range. The IPCE value of the Ru:CeO_x/Sb-TiO_2 photoanode in the 400–550 nm range is significantly higher than that of the Sb-TiO_2 NRs photoanode. This enhanced IPCE of Ru:CeO_x/Sb-TiO_2 is because of the improved visible light abosorption of the photoanode in the same wavelength region (Fig. S6b).

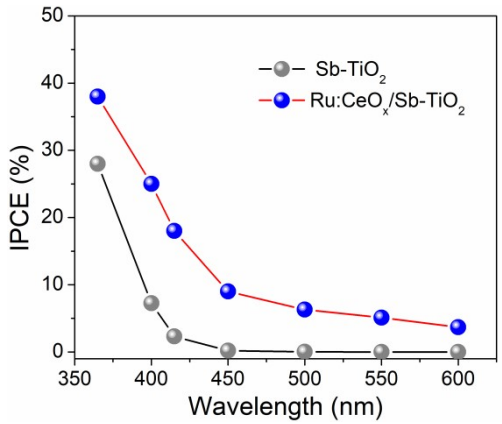

Fig. S8 IPCE plots of the photoanodes measured at 1.23 V_{RHE}.

DFT simulation of OER

Here the computational hydrogen electrode (CHE) model has been adopted [13,14] to investigate the photocatalytic OER performance of pristine CeO_2 (111), and Ru:CeO_2(111) surfaces. In general, OER is four steps process where each step involves one electron transfer. In the first step, the H_2O could be dissociated at the catalytic site under the influence of a photogenerated

hole, and then a proton would be released and the OH* would be formed. In the second step, the OH radical releases another proton and forms the O* with the interaction of a photogenerated hole. In the third step, the O* combines with adjacent H_2O forming the *OOH, releasing a proton. In the final step, the *OOH radical would further release a proton to form O_2, then the O_2 leaves the surface of the photoelectrode. The optimal OER reaction pathways could be described as:

$$H_2O + * \rightleftharpoons OH^* + H^+ + e^- \quad (12)$$

$$OH^* \rightleftharpoons O^* + H^+ + e^- \quad (13)$$

$$O^* + H_2O \rightleftharpoons OOH^* + H^+ + e^- \quad (14)$$

$$OOH^* \rightleftharpoons O_2 + H^+ + e^- \quad (15)$$

Where * stands for the reaction site of the photocatalyst, and OH*, O*, and OOH* refer to adsorbed intermediates in the OER process.

The decisive role for overpotential (η) is determined by the largest Gibbs free energy change (ΔG) among four reaction steps:

$$\eta = -\frac{max\left[\left|\Delta G_{OH^*}\right|, \left|\Delta G_{O^*} - \Delta G_{OH^*}\right|, \left|\Delta G_{OOH^*} - \Delta G_{O^*}\right|, \left|4.92 - \Delta G_{OOH^*}\right|\right]}{e} - 1.23 \quad (16)$$

The calculations of Gibbs free energies without the biased voltage of each step are performed within the framework proposed by Nørskov et al [14,15]:

$$\Delta G = \Delta E + \Delta E_{ZPE} - T\Delta S \quad (17)$$

Here, ΔE is the change in electronic energy, ΔE_{ZPE} is the change of zero-point energy, T is the temperature (298.15 K), and ΔS is the entropy change. The contributions of ZPE and the entropy are determined by calculating the vibrational frequencies. During the frequency calculation, only the adsorbate was calculated explicitly, and the substrate was fixed.

The relationship of Gibbs free energy in the CHE model meets the following conditions:

$$G(H^+) + G(e^-) = \frac{1}{2}G(H_2) \quad (18)$$

$$G(H^+) + G(OH^-) = G(H_2O) \quad (19)$$

$$2G(H_2) + G(O_2) - 2G(H_2O) = 4.92\ eV \quad (20)$$

In this calculation, the free energy of O_2 is obtained by *Eq.* (19) rather than DFT because of the large error in calculating O_2 in VASP program. The structures of adsorbed intermediates (OH*, O*, and OOH*) of pristine CeO_2 (111) and Ru:CeO_2 (111) surfaces are plotted in Fig. S9, S10 and S11. The Ce atoms in the CeO_2 (111) crystal plane were selected as the active site of OER for the pristine CeO_2 (111) catalyst. On the other hand, Ru atoms and Ce atoms neighbouring the Ru atoms were selected as the active sites of OER for Ru:CeO_2 (111) catalyst. The calculated total energy, ZPE, entropy, and Gibbs free energy for all the structures are shown in Table S3, S4, and S5.

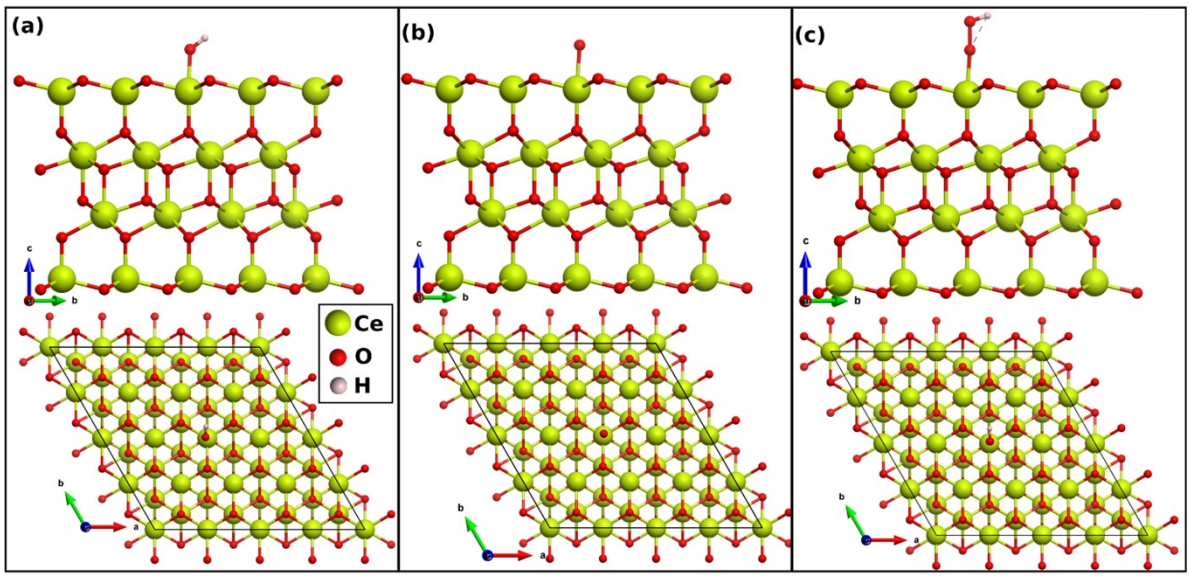

Fig. S9 Side view (upper panel) and top view (lower panel) of the optimized structures of (a) *OH, (b) *O, and (c) *OOH adsorption on the CeO_2 (111) surface. The Ce atom in the CeO_2 (111) surface is the active site.

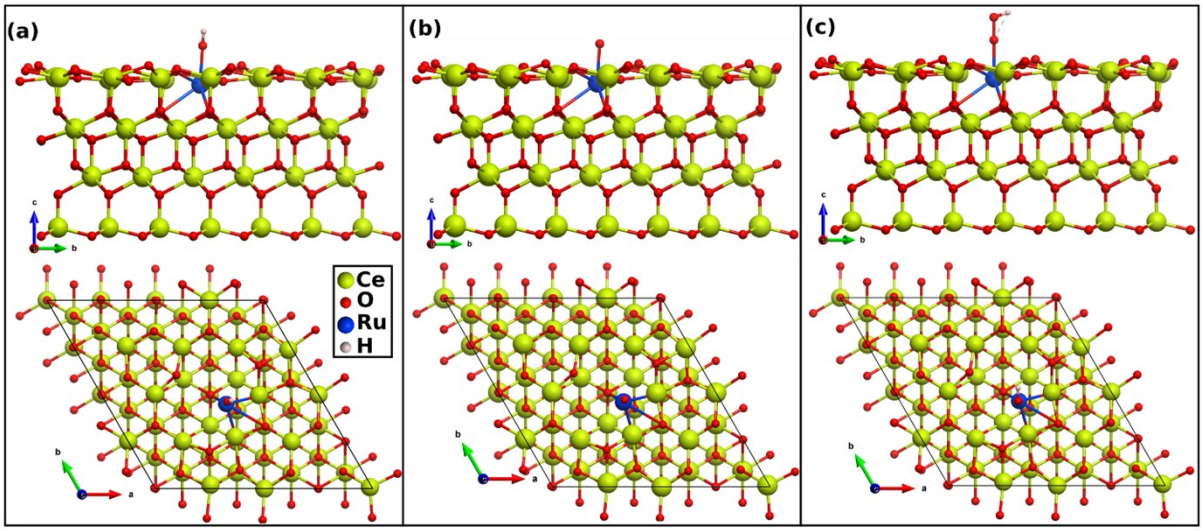

Fig. S10 Side view (upper panel) and top view (lower panel) of the optimized structures of (a) *OH, (b) *O, and (c) *OOH adsorption on the Ru:CeO_2 (111) surface. The Ru atom in the Ru:CeO_2 (111) surface is the active site.

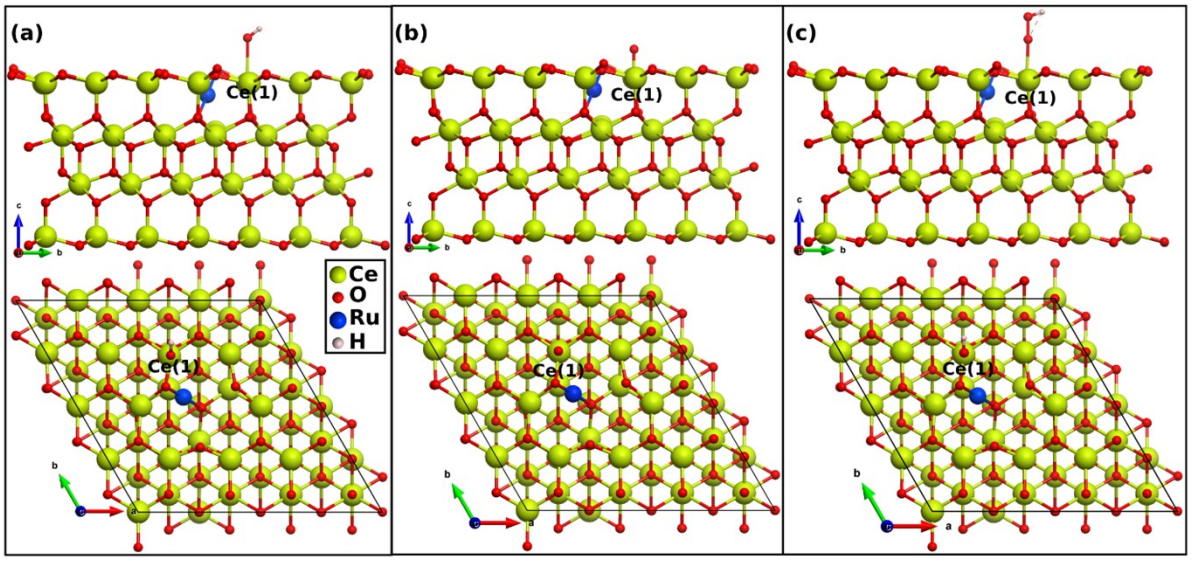

Fig. S11 Side view (upper panel) and top view (lower panel) of the optimized structures of (a) *OH, (b) *O, and (c) *OOH adsorption on the Ru:CeO_2 (111) surface. The Ce atom near the Ru atom in the Ru:CeO_2 (111) surface is the active site.

Table S3 Total Energy, Zero Point Energy, Temperature*entropy of the clean surface, and *OH, *O, and *OOH intermediate adsorbed (at Ce site) surfaces of CeO_2 (111).

Structures	Total Energy (eV)	Zero Point Energy (eV)	T*Entropy (eV)	Free Energy (eV)
Clean CeO_2 (111) surface	−1263.73	0	0	−1263.73
*OH–CeO_2 (111)	−1275.47	0.309506	0.150554	−1275.31
*O–CeO_2 (111)	−1271.57	0.057642	0.086385	−1271.59
*OOH–CeO_2 (111)	−1279.54	0.392961	0.180981	−1279.33

Table S4 Total Energy, Zero Point Energy, Temperature*entropy of clean surface, and *OH, *O, and *OOH intermediate adsorbed (at Ru site) surfaces of Ru:CeO_2 (111).

Structures	Total Energy(eV)	Zero Point Energy (eV)	T*Entropy (eV)	Free Energy (eV)
Clean Ru:CeO_2 (111) surface	−1263.08	0	0	−1263.08
*OH–Ru:CeO_2 (111)	−1275.48	0.348096	0.091881	−1275.22
*O–Ru:CeO_2 (111)	−1272.34	0.068453	0.043403	−1272.32
*OOH–Ru:CeO_2 (111)	−1279.8	0.440923	0.152105	−1279.51

Table S5 Total Energy, Zero Point Energy, Temperature*entropy of clean surface, and *OH, *O, and *OOH intermediate adsorbed (at Ce site neighbour to the Ru atom) surfaces of Ru:CeO_2 (111).

Structures	Total Energy(eV)	Zero Point Energy (eV)	T*Entropy (eV)	Free Energy (eV)
Clean Ru:CeO_2 (111) surface	−1263.08	0	0	−1263.08
*OH–Ru:CeO_2 (111)	−1275.32	0.326954	0.097467	−1275.09
*O–Ru:CeO_2 (111)	−1271.79	0.069544	0.045881	−1271.77
*OOH–Ru:CeO_2 (111)	−1279.99	0.226909	0.095646	−1279.86

References

1 S. Wang, T. He, P. Chen, A. Du, K. (Ken) Ostrikov, W. Huang and L. Wang, *Adv. Mater.*, 2020, **32**, 2001385.
2 C. W. Kim, S. J. Yeob, H.-M. Cheng and Y. S. Kang, *Energy Environ. Sci.*, 2015, **8**, 3646–3653.
3 F. Ning, M. Shao, S. Xu, Y. Fu, R. Zhang, M. Wei, D. G. Evans and X. Duan, *Energy Environ. Sci.*, 2016, **9**, 2633–2643.
4 P. S. Bassi, R. P. Antony, P. P. Boix, Y. Fang, J. Barber and L. H. Wong, *Nano Energy*, 2016, **22**, 310–318.
5 H. Dotan, K. Sivula, M. Grätzel, A. Rothschild and S. C. Warren, *Energy Environ. Sci.*, 2011, **4**, 958–964.
6 L. Wang, N. T. Nguyen, X. Huang, P. Schmuki and Y. Bi, *Adv. Funct. Mater.*, 2017, **27**, 1703527.
7 Y.-C. Pu, G. Wang, K.-D. Chang, Y. Ling, Y.-K. Lin, B. C. Fitzmorris, C.-M. Liu, X. Lu, Y. Tong, J. Z. Zhang, Y.-J. Hsu and Y. Li, *Nano Lett.*, 2013, **13**, 3817–3823.
8 Y. Liu, M. Xia, L. Yao, M. Mensi, D. Ren, M. Grätzel, K. Sivula and N. Guijarro, *Adv. Funct. Mater.*, 2021, **31**, 2010081.
9 G. Wang, H. Wang, Y. Ling, Y. Tang, X. Yang, R. C. Fitzmorris, C. Wang, J. Z. Zhang and Y. Li, *Nano Lett.*, 2011, **11**, 3026–3033.
10 R. A. Parker, *Phys. Rev.*, 1961, **124**, 1719–1722.
11 M. Ye, J. Gong, Y. Lai, C. Lin and Z. Lin, *J. Am. Chem. Soc.*, 2012, **134**, 15720–15723.
12 W. Schottky, *Z. Phys.*, 1942, **118**, 539–592.
13 J. Rossmeisl, Z.-W. Qu, H. Zhu, G.-J. Kroes and J. K. Nørskov, *J. Electroanal. Chem.*, 2007, **607**, 83–89.
14 J. K. Nørskov, J. Rossmeisl, A. Logadottir, L. Lindqvist, J. R. Kitchin, T. Bligaard and H. Jónsson, *J. Phys. Chem. B*, 2004, **108**, 17886–17892.
15 A. A. Peterson, F. Abild-Pedersen, F. Studt, J. Rossmeisl and J. K. Nørskov, *Energy Environ. Sci.*, 2010, **3**, 1311.